Biodegradable Zn-2Cu-0.5Zr alloy promotes the bone repair of senile osteoporotic fractures via the immune-modulation of macrophages

Huanzhong Ji [a,1], Gang Shen [b,1], Hanghang Liu [a], Yao Liu [a], Junyu Qian [b], GuoJiang Wan [b,*], En Luo [a,**]

[a] State Key Laboratory of Oral Diseases & National Center for Stomatology & National Clinical Research Center for Oral Diseases, West China Hospital of Stomatology, Sichuan University, Chengdu, 610041, Sichuan, China
[b] Institute of Biomedical Engineering, College of Medicine/Key Laboratory of Advanced Technologies of Materials, Ministry of Education, Southwest Jiaotong University, Chengdu, 610031, Sichuan, China

ABSTRACT

Delayed bone-healing of senile osteoporotic fractures remains a clinical challenge due to the alterations caused by aging in bone and immune systems. The novel biomaterials that address the deficiencies in both skeletal cells and immune systems are required to effectively treat the bone injuries of older patients. Zinc (Zn) has shown promise as a biodegradable material for use in orthopedic implants. To address the bone-healing deficiencies in elderly patients with bone injuries, we developed a biodegradable Zn-based alloy (Zn–2Cu-0.5Zr) with enhanced mechanical properties, including a yield strength of 198.7 MPa and ultimate tensile strength of 217.6 MPa, surpassing those of pure Zn and Zn–2Cu alloys. Cytotoxicity tests conducted on bone marrow mesenchymal stem cells (BMSCs) and MC3T3-E1 cells demonstrated that the extracts from Zn–2Cu-0.5Zr alloy exhibited no observable cytotoxic effects. Furthermore, the extracts of Zn–2Cu-0.5Zr alloy exhibited significant anti-inflammatory effects through regulation of inflammation-related cytokine production and modulation of macrophage polarization. The improved immune-osteo microenvironment subsequently contributed to osteogenic differentiation of BMSCs. The potential therapeutic application of Zn–2Cu-0.5Zr in senile osteoporotic fracture was tested using a rat model of age-related osteoporosis. The Zn–2Cu-0.5Zr alloy met the requirements for load-bearing applications and accelerated the healing process in a tibial fracture in aged rats. The imaging and histological analyses showed that it could accelerate the bone-repair process and promote the fracture healing in senile osteoporotic rats. These findings suggest that the novel Zn–2Cu-0.5Zr alloy holds potential for influencing the immunomodulatory function of macrophages and facilitating bone repair in elderly individuals with osteoporosis.

1. Introduction

Decreased bone mass and deteriorated bone microarchitecture can be caused by osteoporosis, which significantly raises the risk of fractures [1]. Senile osteoporosis (SOP), predominantly affecting women and men over the age of 65 and 70, has emerged as a significant public health concern in our increasingly aging society [2–4]. Patients with SOP exhibit limited bone regenerative capacity, leading to common complications such as bone non-unions and infections following fractures [5,6]. These complications can result in considerable morbidity, mortality and healthcare expenditures. Therefore, promoting the healing of senile osteoporotic fractures is vital for reducing hospitalization and rehabilitation durations, as well as for mitigating further complications.

Conventional permanent metals, such as stainless steel, cobalt-chromium and titanium alloy, have sufficient mechanical strength and

acceptable biocompatibility for clinical use in fracture fixation. However, these metals pose a heightened risk of re-fracture due to stress-shielding, particularly in patients with osteoporotic fractures [7,8]. Moreover, a second surgery is needed to remove the non-biodegradable implants to prevent potential adverse complications, such as chronic inflammation [9]. On the other hand, recent studies have highlighted macrophage polarization switches from the tissue repair-mediating anti-inflammatory (M2) phenotype to the inflammatory (M1) phenotype with aging [10]. The remodeling of osteoporotic fractures may be hindered because of the rise of pro-inflammatory cytokines and the reduction of osteogenic cytokines [11–13]. Moreover, the osteoclastogenesis and bone resorption can be further triggered [14]. Therefore, an ideal metallic biomaterial for orthopedic applications should possess both biodegradable and immunomodulatory properties to support effective healing and tissue integration.

In recent years, zinc (Zn)-based alloys have shown promise as a biodegradable material in the field of orthopedic implants owing to their advantageous corrosion behavior [15,16]. The osteogenic properties of Zn-based materials have been revealed by the previous studies [17–20]. As the primary product during degradation, the Zn ion can regulate bone remodeling by stimulating osteoblastogenesis and discouraging osteoclastogenesis at the cellular level [21,22]. Furthermore, Zn ion is essential for the metabolism and immune systems in human health [23]. Long-term in vivo studies also have shown that pure Zn metal's degradation products could be safely tolerated and metabolized by the body, indicating the excellent biocompatibility of Zn [17,24].

However, the mechanical properties of pure Zn metal cannot fulfill the requirements for clinical applications. By alloyed with other elements or subjected to thermomechanical treatment, the strength properties of Zn-based metals can be significantly enhanced compared to pure Zn [25]. Among potential alloying elements, copper (Cu) is a promising choice due to its essential role as a trace element for human health. Additionally, incorporating Cu into the Zn matrix improves both strength and ductility while also imparting antibacterial properties [26–29]. To build on the enhancements provided by Cu, the introduction of zirconium (Zr) into the Zn–Cu alloy system represents a strategic advancement. Zr is known for its strong grain-refining capabilities [30], which are hypothesized to synergize with Cu's benefits, potentially leading to alloys with superior mechanical properties. Furthermore, both in vitro and in vivo tests demonstrate that Zr possesses low ionic cytotoxicity and excellent biocompatibility [31].

This study concentrates on creating a novel ZnCuZr alloy system through the incorporation of Cu and Zr into Zn, aiming to enhance its suitability for biodegradable metal applications. The microstructure, mechanical property and biosafety of Zn–2Cu-0.5Zr (97.5 wt% Zn, 2.0 wt% Cu, and 0.5 wt% Zr) alloy was investigated. RAW 264.7 cells were exposed to the extracts from Zn–2Cu-0.5Zr alloy to investigate the impact of the ZnCuZr alloy system on the transformation of macrophage phenotype and production of inflammatory cytokines. Then effects of Zn–2Cu-0.5Zr alloy extracts on the osteogenic differentiation of bone marrow mesenchymal stem cells (BMSCs) via osteo-immunomodulation were investigated using conditioned medium methods. Finally, the potential application of Zn–2Cu-0.5Zr alloy for promoting healing of SOP fractures was further evaluated in the aged rats (see Fig. 1).

2. Materials and methods

2.1. Materials

High-purity metals of Zn (99.99 %), Cu (99.99 %) and Zr (99.99 %) metals were applied to prepare the ZnCuZr alloy system. The metals mentioned above were melt at 680 °C, which were subsequently cast and cooled down to form the alloy ingots of Zn–2Cu and Zn–2Cu-0.5Zr. The obtained ingots were then homogenized at 350 °C and extruded at 300 °C to fabricate the Zn, Zn–2Cu and Zn–2Cu-0.5Zr (based on weight ratios), with the extrusion ratio of 22:1. Specimens of $\Phi 10 \times 1.5$ mm were prepared for microstructure analyses, while the dimension of $30 \times 10 \times 1.5$ mm was adopted for the follow-up cytotoxicity tests. Besides, the cylindrical samples of $\Phi 1.2$ mm were prepared for in vivo analyses. All alloy samples were polished using silicon carbide grinding papers and subsequently cleansed with ethanol and acetone before being air-drying.
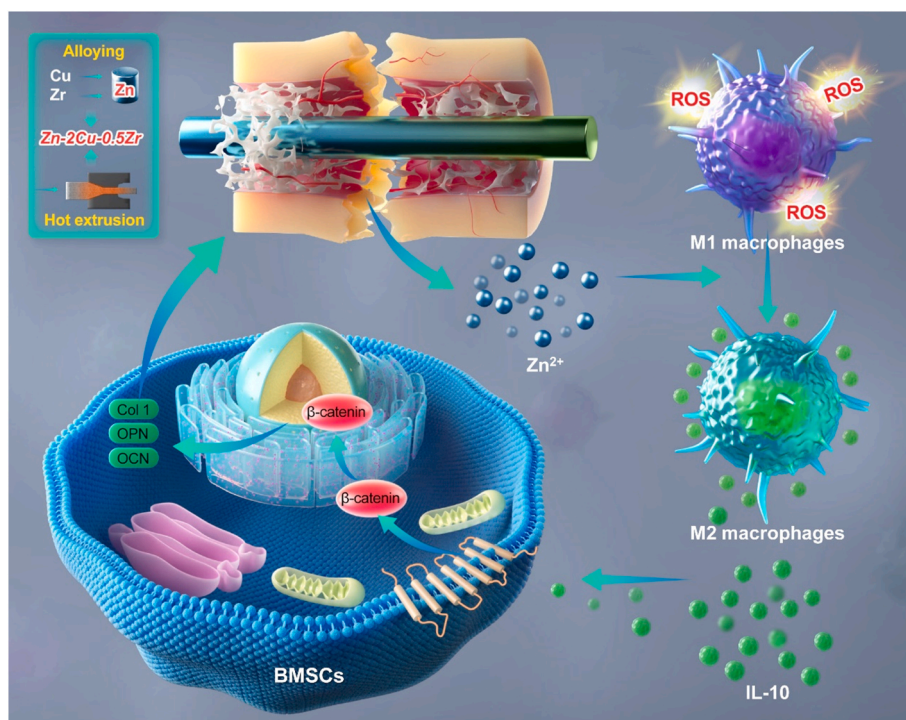
Fig. 1. Schematic diagram illustrating the mechanism of influencing the immune-osteo cascade during bone regeneration and finally facilitating the healing of senile osteoporotic fractures.

2.2. Microstructural characterization

Prior to microstructural examination, the samples were polished using grinding paper and treated with an etch solution. Subsequently, the metallographic structures of the samples were examined under an optical microscope (Motic Images Plus 2.0 ML). For further characterization of the secondary phases, the field-emission scanning electron microscopy (FE-SEM, JSM-7401F, JEOL, Japan) in conjunction with energy dispersive spectroscopy (EDS) was utilized. The phase composition in the samples was examined utilizing the X-ray diffraction (XRD) techniques employing a CuK radiation source. The glancing angle was adjusted at 2° with a step size of 0.25° and a range of 2° from 20° to 90°.

2.3. Mechanical tests

Tensile tests were conducted in accordance with the ASTM E8/E8M-16a standard. A universal testing device (LabTest Instron-5567) was used, while the deformation rate was set at 1 mm/min to assess each sample's mechanical tensile characteristics. Stress-strain curves for three samples per group were analyzed to assess their yield strength (YS), ultimate tensile strength (UTS), and elongation.

2.4. Cytotoxicity assessment

Before performing the cytotoxicity tests, the samples were cleaned with ultraviolet light for 1 h each side for the extract acquisition. Two types of cells (BMSCs and MC3T3-E1 cells) were used. BMSCs were cultivated in α-MEM medium, whereas MC3T3-E1 cells were maintained in DMEM. The corresponding culture medium was used to achieve the extracts with 1.25 cm^2/mL ratio for a duration of 24 h at 37 °C in a humidified 5 % CO$_2$ atmosphere. The concentration of metallic ions in the medium were then measured with an inductively coupled plasma optical emission spectrometer (ICP-OES; Optima 4300DV, Germany). Afterwards, an appropriate amount of serum was supplemented to the sample extracts prior to the subsequent assays. The diluted 50 % and 10 % extracts were utilized for the following experiment.

BMSCs and MC3T3-E1 cells were cultivated in 96-well plates (5000 cells per well). After an overnight culture, the standard α-MEM and DMEM medium were replaced with 50 % and 10 % extracts, which were refreshed every 24 h. Following 1, 3, and 5 days of culture, BMSCs and MC3T3-E1 cells were incubated in 10 % CCK-8 reagent without serum for 40–60 min. Afterwards, an enzymatic marker was used to assess the cell viability at the absorbance of 450 nm.

BMSCs and MC3T3-E1 cells were seeded in 24-well plates (3 × 10^4 cells per well). Standard α-MEM and DMEM medium was replaced with 50 % and 10 % extracts for a duration of 24 h after overnight culture. Then, the cells were rinsed after removing extracts and stained using a live/dead staining reagent (Sigma-Aldrich, Taufkirchen, Germany). Following 10-min incubation in the dark, BMSCs and MC3T3-E1 cells were treated with rhodamine-phalloidin and 4′,6-diamidino-2-phenyl-indole for morphological assessment, according to the manufacturers' protocols.

2.5. Effects of Zn–2Cu-0.5Zr extracts on macrophages

2.5.1. Cytocompatibility test

Zn–2Cu-0.5Zr extracts were prepared as described before. In order to evaluate bone immunomodulatory capacity of diluted extracts from about 5 % to 50 %, Zn^{2+} concentration was measured by ICP-OES. Ultimately, we set the research concentration ranging from 0 to 80 μM (that was 10, 20, 50, and 80 μM precisely measured by ICP-OES). 10, 20, 50, and 80 μM of Zn^{2+} corresponded approximately to 5 %, 10 %, 30 % and 45 % diluted extracts, respectively. To be specific, DMEM culture medium served as the control group (0 μM), while the extracts were diluted with DMEM to create experimental groups with concentrations

of 10, 20, 50, and 80 μM.

RAW 264.7 cells were used and cultivated in 96-well plates with the density of 5000 cells per well. Following an overnight incubation, standard DMEM was displaced with the Zn–2Cu-0.5Zr extracts, which were refreshed every 24 h. Cell survival rates at 24 and 48 h were determined using the CCK-8 reagent. For the cytotoxicity assessment, a live/dead staining assay was carried out on RAW 264.7 cells after exposed to the Zn–2Cu-0.5Zr extracts for 24 h, as previously described.

2.5.2. Expression of inflammation-related genes

The *Escherichia coli* lipopolysaccharide (LPS) was selected in this investigation as the inflammatory stimulus to investigate the effects of Zn–2Cu-0.5Zr extracts on the inflammatory response and phenotypic switching of macrophages. After overnight cultivation of RAW 264.7 cells, the original medium was discarded and the serum-free medium containing LPS (50 ng/mL) was added to induce activation of inflammatory macrophages for 2 h. Then, the RAW 264.7 cells were cleaned with PBS after removing the medium containing LPS and cultured with 0, 10, 20, 50, or 80 μM extracts for another 6 h. Subsequently, total RNA was isolated by TRIzol and used to synthesize complementary DNA by PrimeScript RT Reagent Kit. By using SYBR® Premix ExTaqTM II (Takara, Tokyo, Japan), the gene expression linked to the M1 (*CCR7, iNOS, CD86, TNF-α, IL-1β, IL-6*) and M2 (*IL-10, Arg-1, CD206, CD163*) macrophage phenotypes were measured in triplicate. The primer sequences utilized are shown in Table S1. *GAPDH* was employed as an internal control for the target genes, while the Ct method was utilized for determining the fold change.

2.5.3. Production of reactive oxygen species (ROS)

The ROS Detection Assay Kit (Abcam, Cambridge, UK) was employed for the determination of intracellular ROS levels. Briefly, the medium was eliminated after incubating RAW 264.7 cells with the Zn–2Cu-0.5Zr extracts for 6 h. Then, RAW 264.7 cells were treated with the 2′,7′-dichlorofluorescein diacetate solution in a dark environment for 45 min. Subsequently, the cells were washed and fixed with 4 % para-formaldehyde for 15 min. Fluorescence was measured using a fluorescent microplate reader at an excitation wavelength of 485 nm and an emission wavelength of 535 nm. The afore-mentioned procedures were repeated, and cellular ROS levels were further assessed using a fluorescence microscope.

2.5.4. Expression of inflammation-related protein

After incubating with the Zn–2Cu-0.5Zr extracts for 6 h, RAW 264.7 cells were subsequently cleaned and cultured within a fresh serum-free culture medium for additional 12 h. Afterwards, RAW 264.7 cell were subjected to immunofluorescent staining for CD206 and CCR7 to investigate macrophage polarization in vitro. Briefly, the cells were permeabilized with 0.5 % Triton-X and blocked with 1 % BSA after fixing whithin paraformaldehyde solution. The primary antibodies against CD206 and CCR7 were used for incubating overnight at 4 °C. Then, a fluorescence microscope was employed to capture the images of the cells.

Furthermore, lysates of the cells were prepared for western blotting with antibodies against CD206, CD163, iNOS, and CCR7. The target proteins were detected using horseradish peroxidase-conjugated secondary antibodies.

Additionally, the supernatant samples from the cultures of RAW 264.7 cells that had undergone the above-mentioned treatment were taken. The exocrine inflammatory factor detection of TNF-α, IL-6 and IL-10 was measured using the ELISA kits (R&D, USA). All the kits were used in accordance with the makers' instructions.

2.6. Analysis of macrophage-induced influence on BMSCs

2.6.1. Osteogenic differentiation

BMSCs were co-cultured with conditioned medium (CM) derived

from macrophages. Following a 6-h incubation with Zn–2Cu-0.5Zr extracts, RAW 264.7 cells were washed and cultured with a fresh serum-free medium for another 12 h. The supernatant of culture medium was collected and centrifuged at 14,000 rpm for 30 min to remove residual cells and debris. The treated supernatant was then mixed with fresh culture medium (α-MEM supplemented with 10 % FBS and 1 % penicillin/streptomycin) at a 1:1 ratio to prepare the CM for subsequent experiments. The influence of macrophage-derived immune microenvironment mediated by Zn–2Cu-0.5Zr extracts on osteogenic differentiation of BMSCs was then investigated by co-culturing the BMSCs with each respective CM.

BMSCs were cultured with each CM supplemented with the components of the osteogenic differentiation medium. After 7 and 14 d, total RNA of BMSCs was extracted to determine the expression of ALP, Col1, Runx2, OSX, OPN, OCN via qRT-PCR as described before. Additionally, BMSCs lysates were subjected to western-blot analyses with antibodies against ALP, Col1, Runx2, OSX, OPN, OCN following the methods outlined earlier.

On day 7, the cells were stained with ALP in accordance with the manufacturer's instructions. Alizarin Red S staining was performed to evaluate the mineralization nodules of BMSCs on day 14. BMSCs were cleaned up using distilled water, followed by fixation in paraformaldehyde and air-dry.

2.6.2. Activation of WNT/β-catenin signaling

BMSCs were seeded in the 6-well plates (5000 cells per well) and cocultured with each CM. After 24 h, BMSCs lysates were collected as described before and subjected to western blotting with an antibody against total-β-catenin and phosphorylated-β-catenin. It has been reported that the cell-permeable chelator N,N,N′,N′-tetrakis (2-pyridylmethyl) ethylenediamine (TPEN) significantly abolishes Zn^{2+} influx. To determine whether the Zn–2Cu-0.5Zr extracts-macrophage CM activate the Wnt/β-catenin signaling, TPEN was selected for blocking the effect of Zn^{2+}. Briefly, RAW 264.7 cells were treated with the extracts with or without the TPEN (5 μM) for 6 h, followed by a medium change to fresh serum-free culture medium for an additional 12 h. The CM was subsequently prepared as described before and co-cultured with BMSCs. The β-catenin expression of BMSCs was quantified by Western blot at 12 and 24 h. Additionally, an immunofluorescence assay was conducted for the visualization of β-catenin translocation in BMSCs in response to each CM. After a 24-h treatment with each CM, BMSCs were permeabilized and blocked as described before after fixing whithin paraformaldehyde solution. The cells were then incubated overnight at 4 °C with a rabbit anti-β-catenin antibody, followed by a FITC-conjugated goat anti-rabbit secondary antibody (1:400, Bioworld, USA). The cytoskeleton of BMSCs was stained using rhodamine-Phalloidin (Sigma-Aldrich, USA).

2.7. Animal studies

2.7.1. Establishment of the SOP fracture model

Animal experiments were approved by the Animal Research Committee of Sichuan University. 20-month-old Sprague-Dawley (SD) rats maintained on a low-calcium diet were selected as aged subjects for the study. For orthopedic implantation procedures, the aged rats were anesthetized using pentobarbital sodium. A 2 cm incision was made parallel to the right tibia to expose the middle section. A fracture was created in the tibia using a medical saw, and the fracture was then internally stabilized with intramedullary nails made of either Zn–2Cu-0.5Zr alloy or stainless steel. Care was taken to ensure proper alignment of the fracture line before meticulously closing the wound. The rats were euthanized at 2, 4, or 8 weeks after the implantation to harvest the tibiae for micro-CT and histological analyses. For sequential fluorescent labeling, an intraperitoneal injection of calcein (5 mg/kg) was administered two weeks prior to euthanasia, followed by a dose of xylenol orange (90 mg/kg) one week before euthanasia.

2.7.2. Imaging analyses

The healing of the tibial fracture was evaluated through X-ray imaging and micro-CT scanning. The rats were sacrificed for collecting the right tibiae at 2, 4, and 8 weeks after surgery. The tibiae were X-ray scanned (n = 6 per group) with the following parameters: 65 kV working voltage, 7 mA working current, and 0.06 ms integration time. After that, the implants were removed. Micro-CT (μ-CT80, SCANCO, Switzerland) was performed at the following scanning parameters: 70 kV working voltage, 114 μA working current, 400 ms integration time, and 14 μM resolution. The supplied software was used for three-dimensional (3D) reconstruction, and the callus of the tibial-fracture within 1 mm of the fractured proximal and distal ends is selected as the region of interest (ROI) for calculating the micromorphic parameters of BV, BV/TV, Tb.Th and BMD.

2.7.3. Histological assessment

The tibial fracture samples collected 2, 4, or 8 weeks after the implantation. The samples were decalcified with 10 % EDTA after being fixed in 4 % paraformaldehyde solution. Then, they were embedded and sliced into 5 μm sections for further analysis. The callus around the fractures of the samples collected at 2 weeks was analyzed via immunohistochemical staining for CD206, IL-10, iNOS and IL-6 expression. The sections underwent overnight incubation with the respective primary antibodies at 4 °C. Subsequently, the samples were treated with a horseradish peroxidase-linked secondary antibody. The samples collected at 4 and 8 weeks were subjected to HE and Masson staining according to the instructions of the manufacturers.

The tibial fracture samples were collected 4 or 8 weeks after the implantation. These samples were subjected to the dehydration via graded concentrations of ethanol and embedment in methyl methacrylate after fixing whithin paraformaldehyde solution. After that, the samples were subjected to un-decalcified dissection. Subsequently, the fluorescently labeled sections were imaged using laser scanning confocal microscopy.

2.7.4. Biomechanical test

Tibial fracture samples were collected for a three-point bending test 8 weeks after the surgery. The samples were positioned on two support rods 1.5 cm apart, with the central portion of the tibial callus designated as the test area. The callus region was subjected to compression at a rate of 1 mm/min until fractured. The ultimate load and stiffness of the callus were derived from the load-displacement curve documented by system software.

2.8. Statistical analysis

All the quantitative are presented as mean ± standard deviation (SD). Statistical differences were conducted using Student's *t*-test or one-way analysis of variance (ANOVA) with Tukey's post hoc test in the SPSS software. A *p*-value <0.05 was set as statistically different.

3. Results

3.1. Microstructural and mechanical properties of the Zn alloys

The microstructures of extruded Zn alloys were characterized via optical microscopy and SEM in Fig. 2a. The second-phase particles can be observed within the Zn matrix after the addition of the Cu element. The grain size of Zn matrix phase around the second-phase particles is significantly smaller than that far away. The addition of Cu and Zr element resulted in the formation of new second-phase particles with larger size (10–20 μm) and more regularly shape in the Zn–2Cu-0.5Zr alloy. It can be observed that the number of second-phase particles in the matrix increased, leading to a more intense deformation zone around them and further grain refinement. The secondary phase was characterized by the XRD spectroscopy (Fig. 2b). The results revealed that
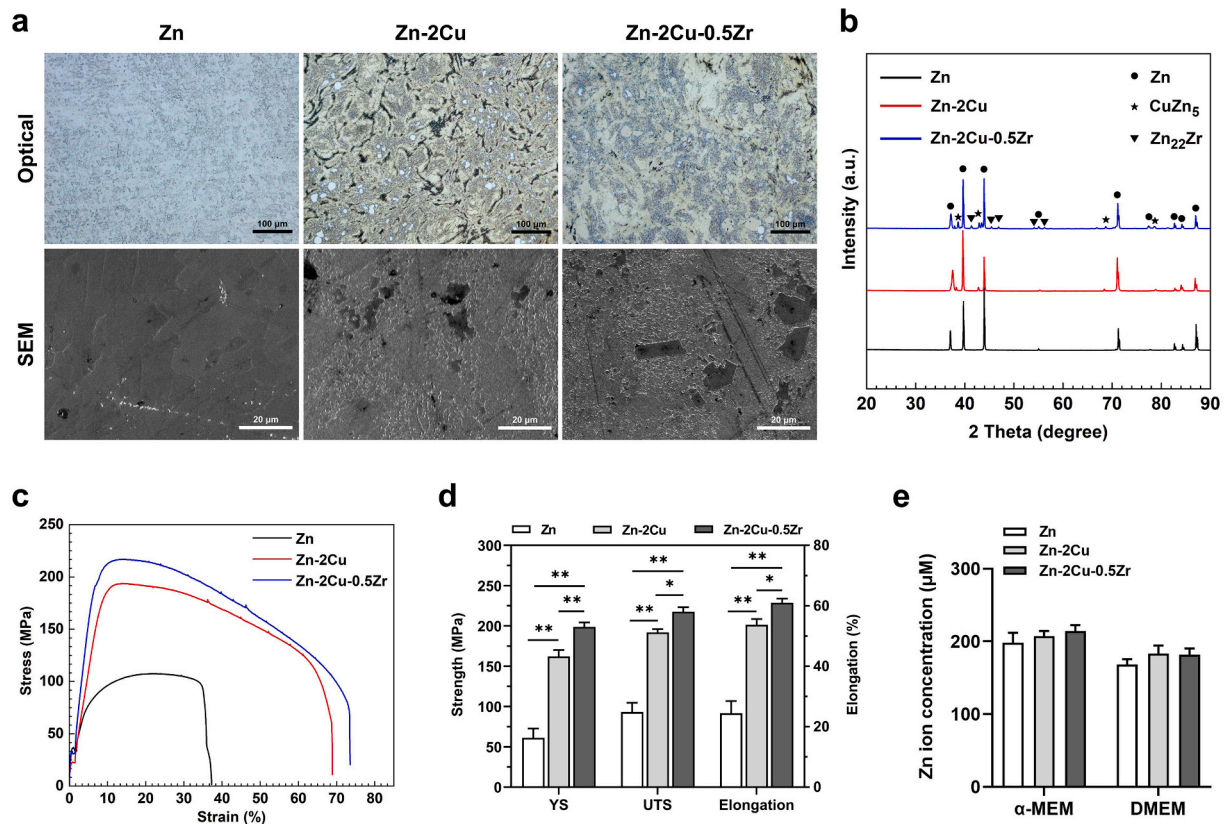
Fig. 2. Microstructure and mechanical properties of Zn–2Cu-0.5Zr alloys. **(a)** SEM and optical images of extruded Zn, Zn–2Cu and Zn–2Cu-0.5Zr alloys. **(b)** X-ray diffraction test of extruded Zn, Zn–2Cu and Zn–2Cu-0.5Zr alloys. **(c)** Representative stress-strain curves of Zn, Zn–2Cu and Zn–2Cu-0.5Zr alloys. **(d)** The yield strength (MPa), ultimate tensile strength (MPa) and elongation at fracture (%) of Zn, Zn–2Cu and Zn–2Cu-0.5Zr alloys. Results are shown as mean ± SD. Comparisons were determined by one-way ANOVA with Tukey's post hoc test (*P < 0.05, **P < 0.01). **(e)** ICP-OES detection of zinc ion concentration of Zn, Zn–2Cu and Zn–2Cu-0.5Zr alloy extract.

Zn–2Cu is mainly composed of Zn matrix and $CuZn_5$. Consequently, the Cu-containing secondary phase could be recognized as $CuZn_5$. The peak intensity of $Zn_{22}Zr$ considerably increased with the addition of Zr, correlating with the larger second-phase particles in the microstructure observation. The chemical composition of the second phase in Zn–2Cu and Zn–2Cu-0.5Zr is indicated (Figs. S2a and b). According to the EDS data, the secondary phase in the ZnCuZr alloy system primarily consisted of Zn, Cu, Zr and O elements.

The tensile mechanical properties are shown in Fig. 2c and d. Among the three groups, pure Zn exhibited the lowest YS and UTS values, which were 61.5 and 93.6 MPa respectively. These values were significantly enhanced upon alloying with Cu, reaching YS and UTS of 162.1 MPa and 192.3 MPa, respectively. The Zn–2Cu-0.5Zr alloy system demonstrated superior tensile strength upon the addition of Cu and Zr elements, with YS reaching 198.7 MPa and UTS reaching 217.6 MPa. Additionally, the elongation of ZnCuZr alloy system was 61.8 %, notably higher than that of pure Zn (24.2 %) and ZnCu alloy (54.5 %).

The release of Zn ion in the extracts was quantified using an ICP-OES. The results showed that the concentration of Zn^{2+} released from Zn–2Cu-0.5Zr groups in α-MEM or DMEM had no significant difference compared with Zn and Zn–2Cu. Only the release of Zn^{2+} was detected via the ICP-OES, whereas the metallic ions of Cu and Zr were not measurable, possibly due to their very low level in the alloy (below the detection limit).

3.2. Cytotoxicity evaluation

The fluorescent live/dead imaging of BMSCs and MC3T3-E1 cells co-cultured with the extracts is displayed in Fig. 3a–e. When cultured with

50 % diluted extracts, all the cells exhibited green fluorescence, indicating preserved cell-membrane integrity. The viability of the cells was comparable to the control group, demonstrating that the extracts from all three groups exhibited no significant cytotoxicity. Results of the cytoskeletal actin staining are shown in Fig. 3b–f. BMSCs and MC3T3-E1 cells cultured with 50 % diluted extracts from Zn, ZnCu, and ZnCuZr alloys maintained well-defined spindle-shaped attachments, suggesting that the extracts did not adversely affect cellular morphology.

The outcomes of the CCK-8 assays are illustrated (Fig. 3c, d, g, h), highlighting the effects of the sample extracts on the survival of BMSCs and MC3T3-E1 cells. The data reveal that both 50 % and 10 % diluted extracts had no significant impact on survival rates, with evident cell proliferation observed over time, indicating the absence of cytotoxic effects from the extracts. Furthermore, no significant differences were noted among the Zn, Zn–2Cu and Zn–2Cu-0.5Zr alloy extracts ($p > 0.05$).

3.3. Cytocompatibility and immunomodulatory effects on the macrophages

To explore the bone immunomodulatory potential of extracts from the Zn–2Cu-0.5Zr alloy, we established a range of Zn^{2+} concentrations from 0 to 80 μM, precisely measured via ICP-OES. Initially, we conducted cytocompatibility tests on macrophages to assess the biocompatibility of the selected concentrations. Live/dead imaging of RAW 264.7 cells treated with 0–80 μM Zn^{2+} extracts from Zn–2Cu-0.5Zr alloy predominantly displayed green fluorescence, demonstrating the intact cell-membrane integrity (Fig. 4a). According to the CCK-8 analysis, the survival rate of RAW 264.7 cells remained unaffected by Zn^{2+}
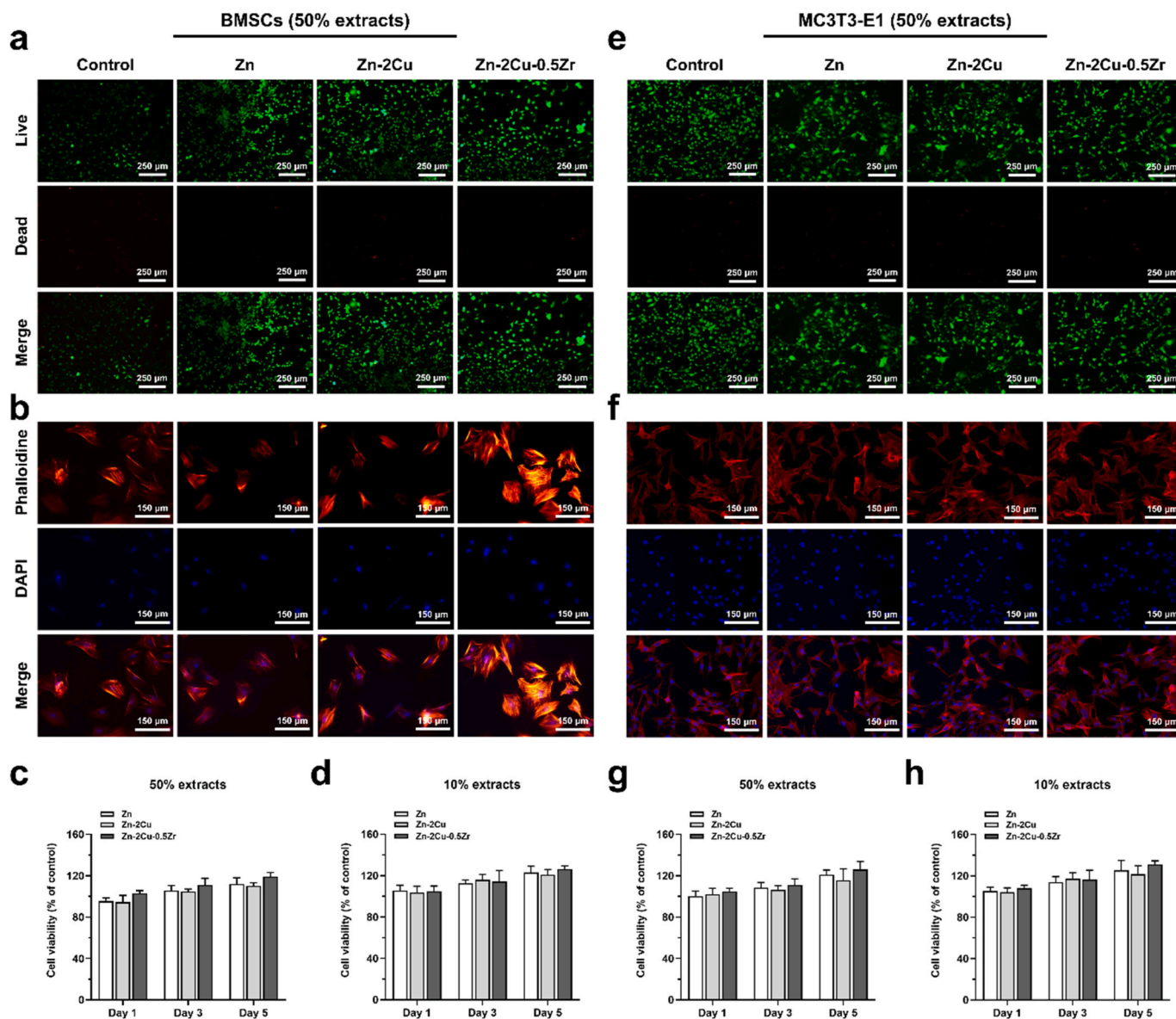
Fig. 3. Cytotoxicity assessment of 50 % extracts and 10 % extracts of Zn, Zn–2Cu and Zn–2Cu-0.5Zr alloys. **(a, e)** The live/dead fluorescent images of BMSCs or MC3T3-E1 cells cultured in 50 % extracts. **(b, f)** The cytoskeletal staining images of BMSCs or MC3T3-E1 cells cultured in 50 % extracts. **(c, d, g, h)** CCK-8 results of BMSCs or MC3T3-E1 cells cultured in 50 % and 10 % extracts at day 1, 3 and 5. Results are shown as mean $\pm$ SD. Comparisons were determined by one-way ANOVA with Tukey's post hoc test.

concentration ranging from 0 to 80 μM in the presence of Zn–2Cu-0.5Zr alloy, with a marked increase in cell proliferation observed over time (Fig. 4b and c). Furthermore, no significant differences in cellular proliferation were noted among the RAW 264.7 cells exposed to Zn^{2+} extracts across the tested concentration range (p > 0.05), indicating that the Zn–2Cu-0.5Zr alloy exhibited no cytotoxic effects on RAW 264.7 cells within the tested range.

To investigate the immunomodulatory properties of the ZnCuZr alloy system, *E. coli* LPS, a polysaccharide and can trigger a strong immune response, was used to simulate inflammatory conditions. The M1 phenotype of macrophages can be induced by LPS to produce pro-inflammatory cytokines such as IL-1β, IL-6 and TNF-α. The macrophage phenotypic response was assessed using qRT-PCR, ELISA and western blotting techniques.

Fig. 5 illustrates the significant influence of Zn–2Cu-0.5Zr extracts on macrophage polarization towards the M1/M2 phenotype, correlating with the concentration of Zn ions. Results from qRT-PCR analysis revealed that LPS triggering prominently boosted the expression of *IL-*

1β, IL-6, TNF-α, CCR7, iNOS and *CD86* (Fig. 5a). However, 20–80 μM Zn^{2+} extracts could significantly mitigate these effects. Notably, the enhance effect of 20–80 μM Zn^{2+} extracts on *Arg-1*, *IL-10*, *CD163* and *CD206* were more pronounced, with lower concentrations failing to demonstrate a significant impact (Fig. 5a). ELISA results supported these findings, showing that 20–80 μM Zn^{2+} extracts increased IL-10 production while reducing levels of TNF-α and IL-6 relative to the control (Fig. 5b). Western blot analysis presented in Fig. 5c showed that these Zn^{2+} concentration extracts suppressed the expression of iNOS and CCR7, while upregulating the markers of M2 macrophages including CD206 and CD163. Immunofluorescence staining of the cells further confirmed significant inhibition of CCR7 and enhancement of CD206 in the groups of 50 and 80 μM Zn^{2+} extracts (Fig. 5d). Additionally, the ROS levels of the cells significantly declined in the 50 and 80 μM groups after 6 h of co-culture, indicating that the Zn ion extract counteracted the upregulation of inflammatory factors including ROS in macrophages stimulated with LPS (Fig. 5e and f).
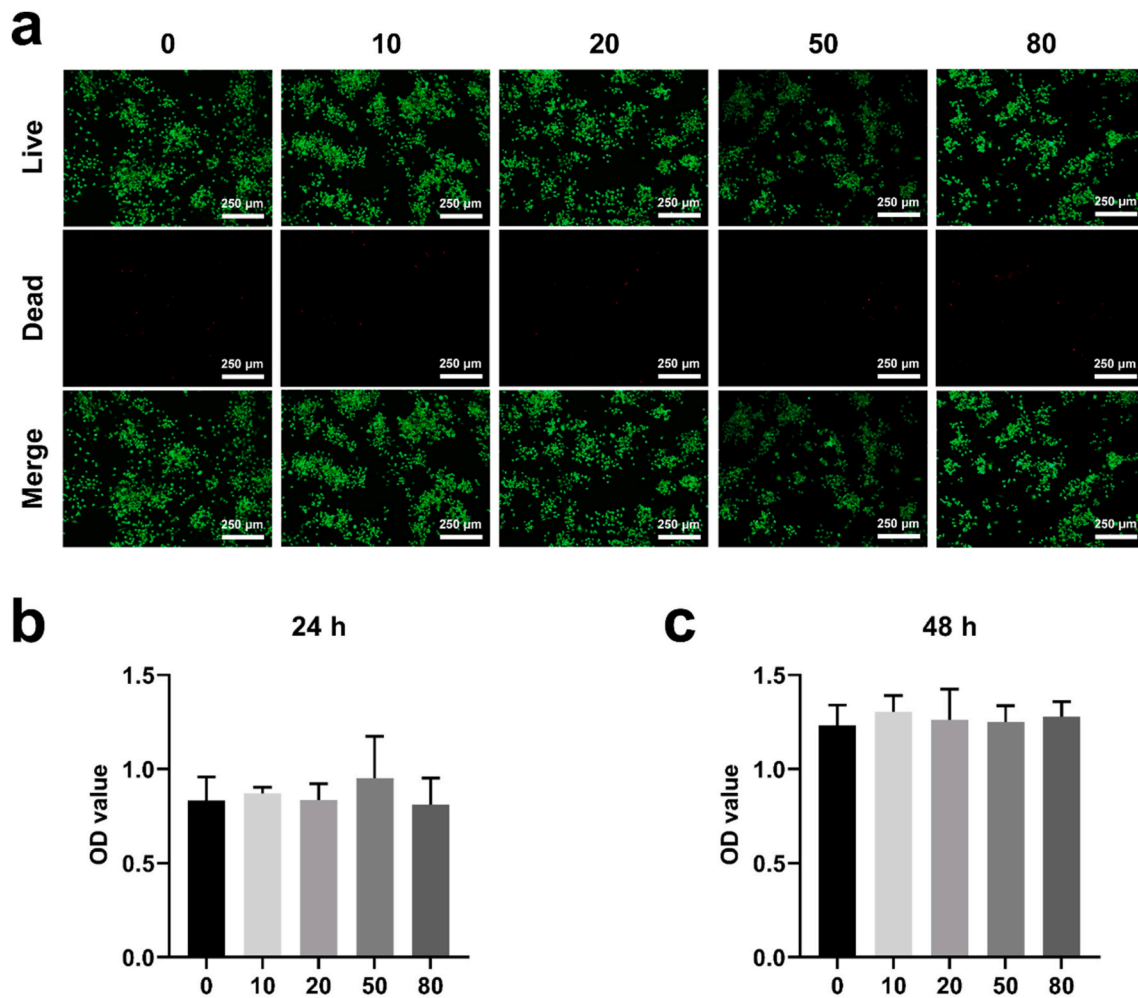
Fig. 4. Cytocompatibility test of 0–80 μM Zn^{2+} extracts from Zn–2Cu-0.5Zr alloy on RAW 264.7 cells. **(a)** The live/dead fluorescent images of macrophage cultured in 0–80 μM Zn^{2+} extracts. **(b)** CCK-8 results of macrophage cultured in 0–80 μM Zn^{2+} extracts at 24 h and 48 h. Results are shown as mean ± SD. Comparisons were determined by one-way ANOVA with Tukey's post hoc test.

3.4. Osteogenic differentiation of BMSCs stimulated by the macrophage-mediated osteo-immune environment

We investigated the osteogenic differentiation of BMSCs stimulated by the CM to elucidate an osteo-immune environment mediated by Zn^{2+} extracts. Fig. 6a shows the osteogenesis-related gene expression in BMSCs. There was a significant upregulation of both early-stage (*ALP*, *Col1*, *Runx2*, and *OSX*) and late-stage (*OCN* and *OPN*) osteogenesis-related genes in the 20, 50 and 80 μM Zn-macrophage CM groups. Western blot analysis further confirmed these findings at the protein level, demonstrating upregulation across these factors (Fig. 6b). ALP staining revealed that after 7 days of osteogenic induction, enhanced ALPase activity can be found in the 10, 20, 50, and 80 μM Zn-macrophage CM groups, with the 20 and 50 μM concentrations exhibiting the most pronounced effects compared to the control (Fig. 6c). Furthermore, results from alizarin red staining showed that after 14 d of osteogenic induction, the number of calcium nodules in the 10, 20, 50, and 80 μM Zn-macrophage CM groups significantly increased, with the 50 and 80 μM showing the most significant effects, compared with the number in the control group (Fig. 6d).

3.5. The involvement of WNT/β-catenin pathway during BMSCs' osteogenic differentiation

Fig. 7a depicts the CM effect on the expression of β-catenin during the osteogenic differentiation of BMSCs. It is evident that the levels of phosphorylated β-catenin in the Zn-macrophage CM significantly increased within the first 24 h of osteogenic induction in BMSCs, particularly in the 20, 50 and 80 μM groups, with the most marked expression observed in the 50 μM group. These results suggest that the Zn-macrophage CM effectively activates the Wnt/β-catenin signaling pathway during osteogenic differentiation, leading to enhanced nuclear translocation of β-catenin.

To verify whether Zn-macrophage CM activates Wnt/β-catenin signaling, we utilized a 50 μM Zn^{2+} extract in the following experiments. Prior research has indicated that the chelating agent TPEN can suppress Zn^{2+} influx, effectively obstructing the action of Zn^{2+}. The level of phosphorylated β-catenin was prominently elevated in 50 μM group compared with the control, suggesting that Zn-macrophage CM activates Wnt/β-catenin signaling during BMSCs' osteogenic differentiation. However, after the addition of TPEN, the level of phosphorylated β-catenin in the Zn^{2+} 50 μM + TPEN 5 μM group was significantly reduced, pointing to a cessation of Wnt/β-catenin signaling upon blocking Zn^{2+} activity (Fig. 7b). Furthermore, immunofluorescence staining of BMSCs revealed a significant increase in nuclear β-catenin in Zn^{2+} 50 μM group, indicating that Zn-macrophage CM can effectively induce the nuclear translocation of β-catenin. Nonetheless, this effect was notably diminished following the addition of TPEN (Fig. 7c). These observations confirm that Zn-macrophage CM can activate Wnt/β-catenin signaling during the osteogenic differentiation of BMSCs.
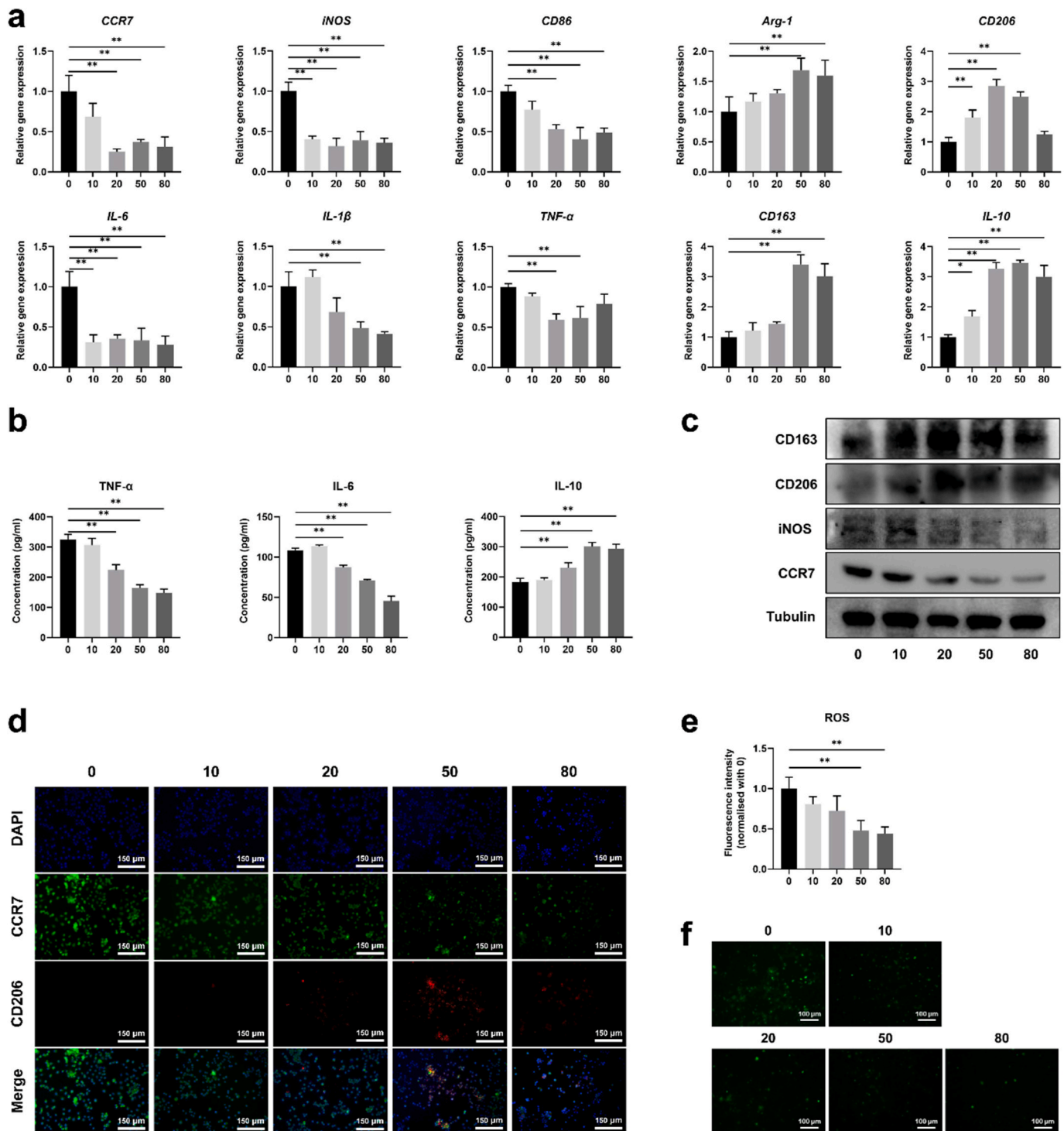
Fig. 5. The immunomodulatory effects of Zn^{2+} extracts on macrophage inflammatory response and polarization. **(a)** The gene expression of *TNF-α, IL-1β, IL-6, CCR7, iNOS, CD86, Arg-1, IL-10, CD163* and *CD206* determined by qRT-PCR under stimulation of Zn^{2+} extracts. Results are shown as mean ± SD. Comparisons were determined by one-way ANOVA with Tukey's post hoc test (*P < 0.05, **P < 0.01). **(b)** TNF-α, IL-6 and IL-10 secretion in the culture media was detected by ELISA. Results are shown as mean ± SD. Comparisons were determined by one-way ANOVA with Tukey's post hoc test (**P < 0.01). **(c)** Western blot of CD163, CD206, iNOS and CCR7 in macrophage under stimulation of Zn^{2+} extracts. **(d)** Representative images of CD206 and CCR7 immunofluorescence staining of macrophage. **(e)** ROS production of macrophage under stimulation of Zn^{2+} extracts. Results are shown as mean ± SD. Comparisons were determined by one-way ANOVA with Tukey's post hoc test (**P < 0.01). **(f)** Representative images of ROS immunofluorescence staining of macrophage.

3.6. Imaging analyses of fracture healing in aged osteoporotic rats

The findings of SOP rat model revealed a notable reduction of trabeculae near the tibial epiphysis in aged rats compared to younger counterparts, as confirmed by micro-CT as well as HE staining (Figs. S3a-

c). Additionally, a significant increase of pro-inflammatory factors (IL-6 and TNF-α) in the serum of aged rats was observed, with levels being 3.5 and 3 times higher respectively than that of the younger (Fig. S3d). The production of anti-inflammatory factor such as IL-10 exhibited a significant decrease as aging, as depicted in Fig. S3d. These results
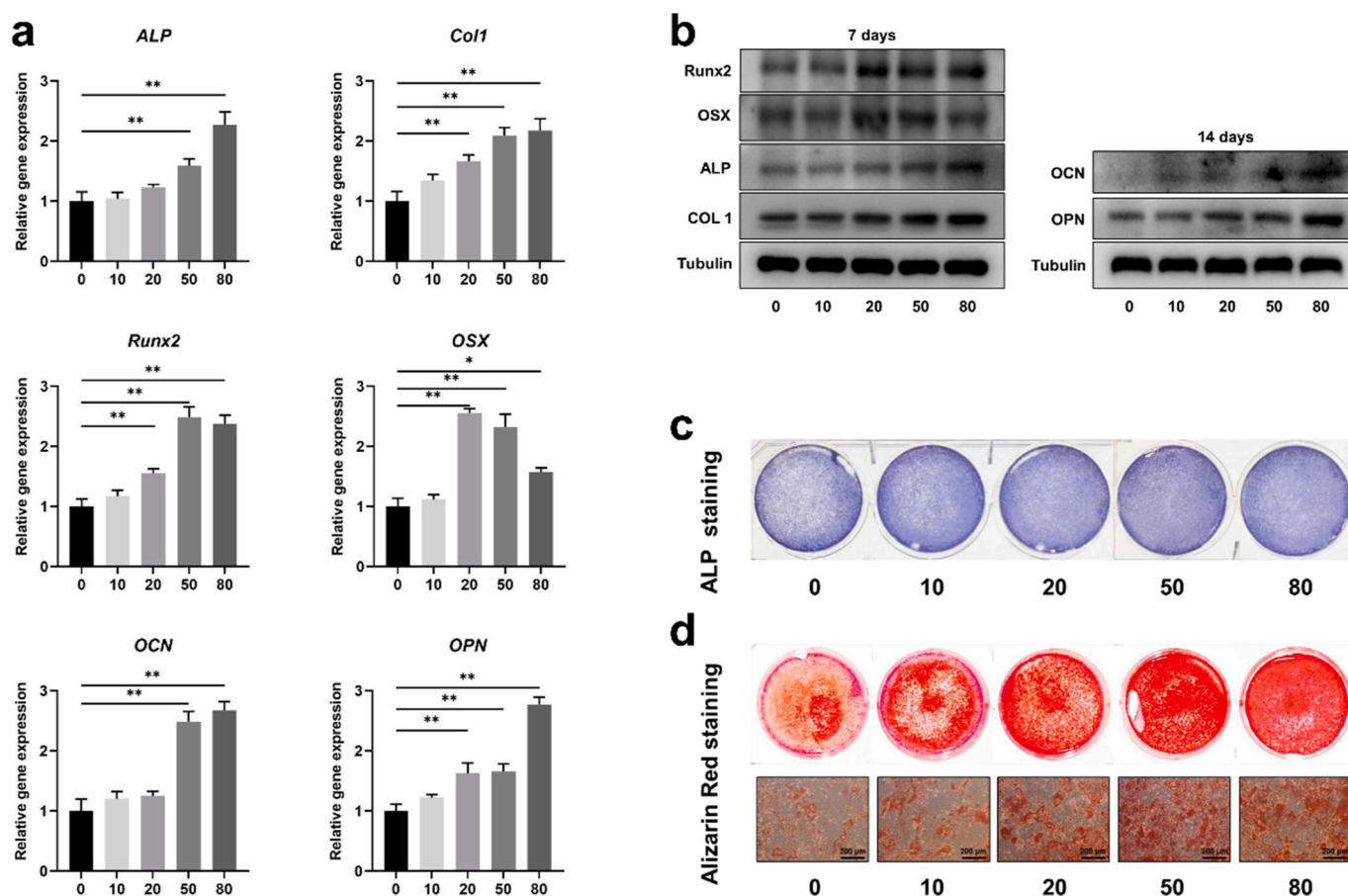
Fig. 6. Osteogenic differentiation of BMSCs under the stimulation of the macrophage modulated osteo-immune environment. **(a)** The gene expression of *ALP, Col1, Runx2, OSX, OCN* and *OPN* determined by qRT-PCR under stimulation of macrophage conditioned medium. Results are shown as mean $\pm$ SD. Comparisons were determined by one-way ANOVA with Tukey's post hoc test (*P < 0.05, **P < 0.01). **(b)** Western blot of ALP, Col1, Runx2, OSX, OCN and OPN in BMSCs under stimulation of macrophage conditioned medium. **(c)** Representative images of ALP staining of BMSCs at day 7. **(d)** Representative images of Alizarin Red staining of BMSCs at day 14.

suggested a shift toward inflammation when aging.

Fig. 8a presents the X-ray results of osteoporotic tibial fracture in aged rats 2, 4, and 8 weeks after the surgery. Overall, the X-ray images from these time points indicated a more rapid healing process in the Zn–2Cu-0.5Zr group. After 2 weeks post-surgery, there was no significant disparity observed in the fracture healing gap between the control and Zn–2Cu-0.5Zr group. However, a greater extent of callus formation surrounding the fracture site was evident in the Zn–2Cu-0.5Zr group compared with the control. At 4 weeks post-surgery, noticeable mineralized callus connections were observed within the fracture area in the Zn–2Cu-0.5Zr group. The callus covered both ends of the fracture, and the broken end at the fracture site was not obvious. Additionally, no clear fracture gap was visible. In contrast, the control group still displayed a clear gap between the ends of the fracture. At 8 weeks after the surgery, the fracture in the Zn–2Cu-0.5Zr group had fully healed, with the two ends completely connected through newly formed bone tissue, leaving no visible gap. Although the fracture gap in the control group had narrowed by the 8-week point compared to the 4-week mark, the X-ray image still indicated the presence of a gap.

Subsequently, the fracture fixation implant was carefully removed and the tibial fracture specimen was analyzed via micro-CT. As shown in Fig. 8b, the control and Zn–2Cu-0.5Zr group 2 weeks after the surgery showed no significant difference. However, at 4–8 weeks post-surgery, micro-CT analysis revealed that the Zn–2Cu-0.5Zr group exhibited superior bone regeneration within the fracture area, accompanied by an accelerated healing process. At 4 weeks after surgery, the fracture area in the Zn–2Cu-0.5Zr group had been bridged by de novo bone tissue,

with a callus encompassing both ends of the fracture and no discernible fracture gap. Two-dimensional tomography images and three-dimensional reconstruction images from the micro-CT scans supported this result. In contrast, the control group exhibited a smaller callus area around the fracture, and the gap between the two ends of the fracture remained clearly visible. At 8 weeks after the surgery, the tibial fracture in the Zn–2Cu-0.5Zr group had completely healed, while the control group still displayed an area not covered by callus with the fracture gap still evident.

The micro-CT analysis of bone tissue parameters demonstrated that the Zn–2Cu-0.5Zr group exhibited higher values for BV, BV/TV, Tb.Th and BMD compared with the control group at 2 weeks post-surgery, although these differences did not reach statistical significance (Fig. 8c). By 4 weeks post-surgery, significant improvements were evident in the Zn–2Cu-0.5Zr group with regard to BV, BV/TV, Tb.Th and BMD, showing statistically significant differences ($p < 0.05$). At 8 weeks post-surgery, the parameters BV and BV/TV continued to be significantly higher in the Zn–2Cu-0.5Zr group ($p < 0.05$), indicating sustained enhancement of fracture healing and bone tissue regeneration around the fracture site. These findings from the micro-CT analysis were consistent with the X-ray images, corroborating that the Zn–2Cu-0.5Zr group effectively promoted the healing of tibial fractures in aged osteoporotic rats.

3.7. Histological assessment of fracture healing in aged osteoporotic rats

To investigate the impact of the Zn–2Cu-0.5Zr implant on the host
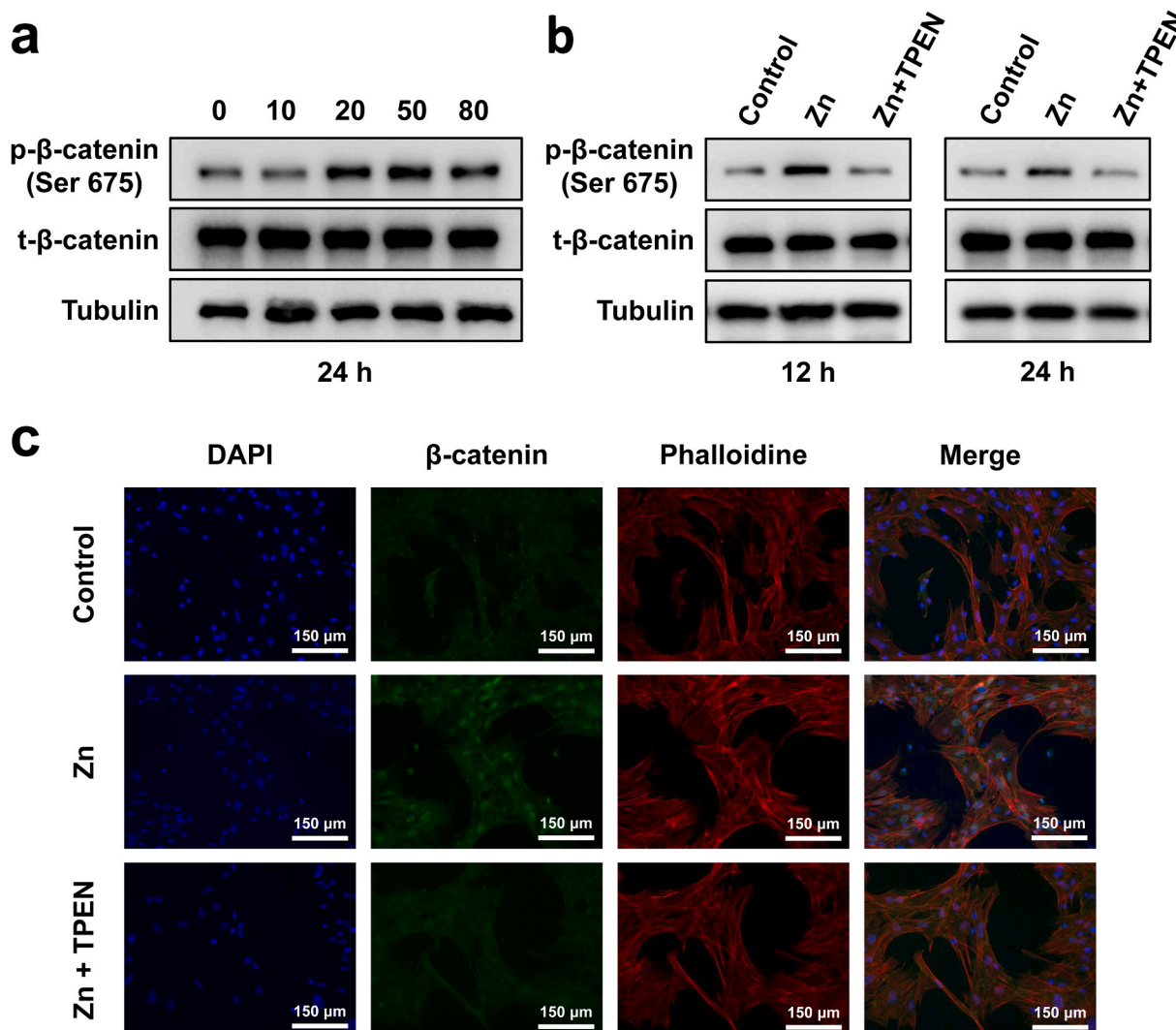
Fig. 7. The involvement of WNT/β-catenin pathway during macrophage-mediated osteogenic differentiation. **(a)** The effect of Zn-macrophage conditioned medium on β-catenin protein expression during osteogenic differentiation of BMSCs cells at 24 h. **(b)** The effect of Zn-macrophage conditioned medium on β-catenin protein expression during osteogenic differentiation of BMSCs cells at 12 and 24 h with the addition of TPEN. **(c)** Representative images of β-catenin immunofluorescence staining of BMSCs.

inflammatory response during fracture healing, we analyzed the expression of inflammatory mediators in the fracture area via immunohistochemistry (Fig. 9a and b). Immunohistochemical staining for inflammation-related proteins revealed that the Zn–2Cu-0.5Zr group had considerably less iNOS positive cells and IL-6 positive cells than the control group 2 weeks after surgery. Furthermore, there was also an increase in the secretion of the anti-inflammatory factors CD206 and IL-10 in the Zn–2Cu-0.5Zr group ($p < 0.05$).

Histological analysis of tibial fractures 4–8 weeks after the surgery, conducted using HE and Masson staining, revealed callus formation, intramembranous ossification and intrachondral ossification in all samples (Fig. 9c and d). The fracture ends were not fully connected in the control or Zn–2Cu-0.5Zr group 4 weeks after the surgery. However, the Zn–2Cu-0.5Zr group displayed more extensive woven bone formation around the fracture site and larger callus area. The surrounding de novo bone tissue exhibited an outstanding increase in the Zn–2Cu-0.5Zr group compared with the control, with enhanced intraperiosteal and intrachondral ossification activities. At 8 weeks after the surgery, the callus area in the Zn–2Cu-0.5Zr group had undergone substantial transformation, with the woven bone replacing the cartilage. This woven bone then progressed to mature, laminated plate bone, ultimately forming a continuous connection across the fracture site. The fracture in

the Zn–2Cu-0.5Zr group had completely healed, with the two ends of the fracture fused together. In contrast, the control group still exhibited an unhealed gap, with cartilage tissue visible in the middle of the fracture, indicating a delayed healing process.

The specimens were dynamically monitored for changes in bone tissue morphology and de novo bone formation through sequence-fluorescent labeling. The markers, calcein (green) and xylenol orange (red), were used to indicate bone growth at 4 and 8 weeks post-surgery, as shown in Fig. 10. We observed that the volume of de novo bone formation in the fracture callus of both the control and Zn–2Cu-0.5Zr groups peaked at week 4 and subsequently decreased by week 8. In cross-sectional comparison, the Zn–2Cu-0.5Zr group had more calcein and xylenol orange markers at 4 and 8 weeks than the control group, indicating that the Zn–2Cu-0.5Zr could promote the osteogenesis around the fracture ($p < 0.05$). These sequence fluorescent labeling assays demonstrate that implantation of Zn–2Cu-0.5Zr enhances both the composition and the mineralization rates of bone.

3.8. Mechanical detection of fracture healing in aged osteoporotic rats

The results of biomechanical testing conducted on tibial fractures are presented in Fig. 11, focusing on ultimate load and stiffness. The
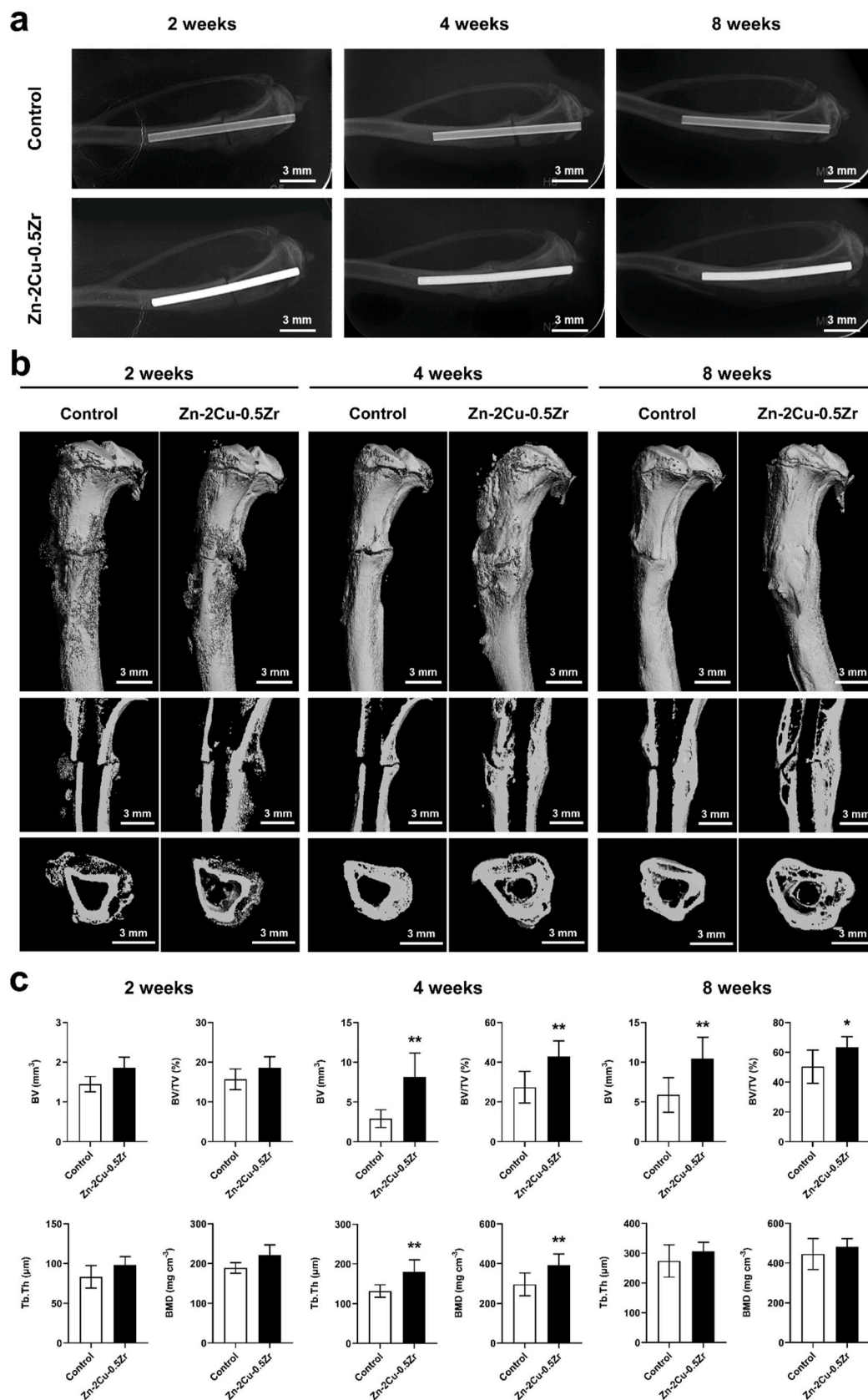
Fig. 8. Imaging examination of fracture healing in aged osteoporotic rats. **(a)** Representative X-ray images of the fractured rat tibia at 2, 4 and 8 weeks after Zn–2Cu-0.5Zr alloy implantation. **(b)** Representative 2D and 3D micro-CT images of the fractured rat tibia at 2, 4 and 8 weeks after Zn–2Cu-0.5Zr alloy implantation. **(c)** The quantitative analysis of BV, BV/TV, Tb.Th and BMD of the fractured rat tibia at 2, 4 and 8 weeks after Zn–2Cu-0.5Zr alloy implantation. Results are shown as mean $\pm$ SD. Comparisons were determined by Student's *t*-test (*P $<$ 0.05, **P $<$ 0.01).
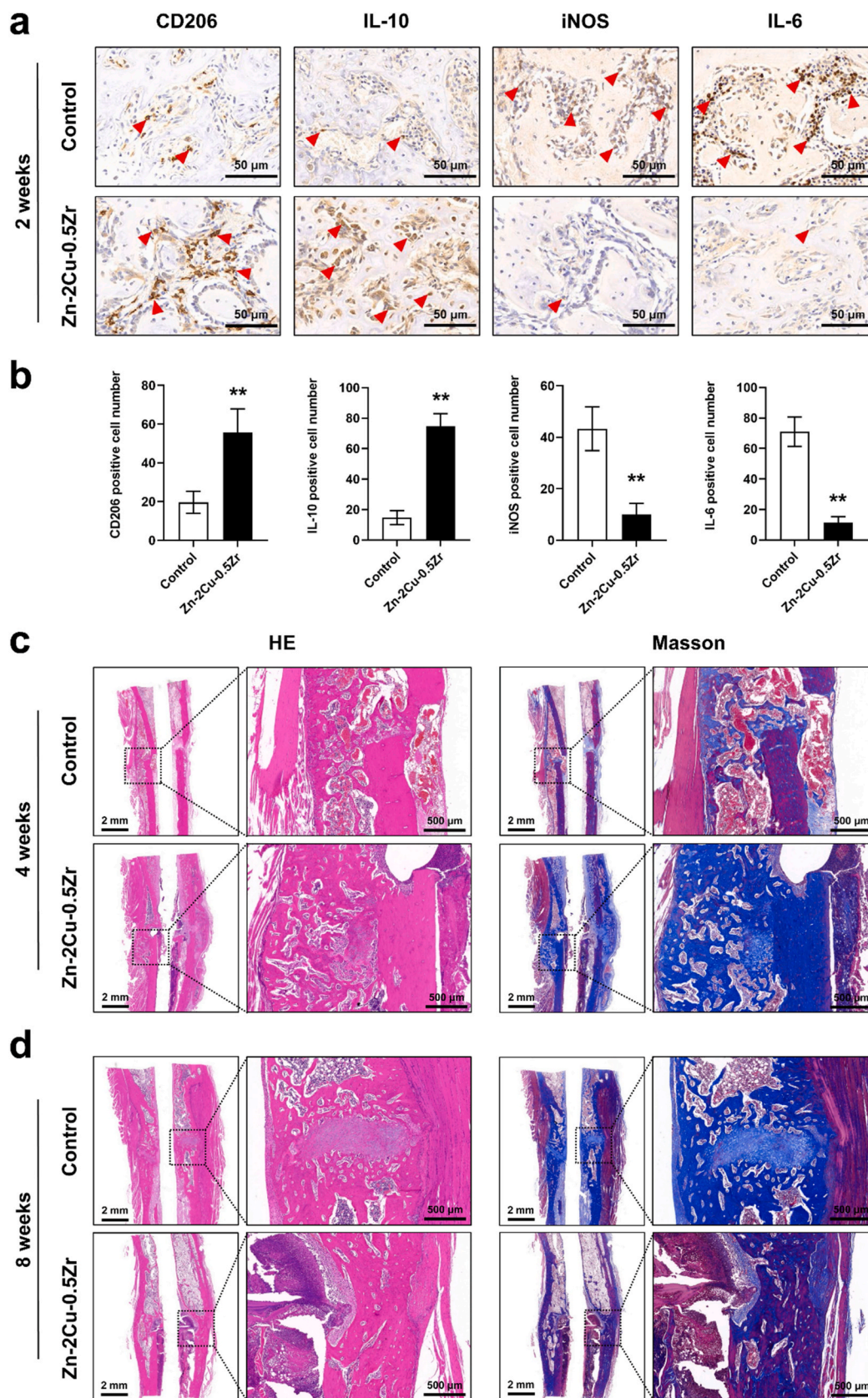
Fig. 9. Histology of fracture healing in aged osteoporotic rats. **(a)** Representative images of CD206, IL-10, iNOS and IL-6 immunohistochemical staining from callus samples around tibial fractures at 2 weeks after surgery. The red arrows show the positive cells. **(b)** The quantitative analysis of the CD206, IL-10, iNOS and IL-6 positive cell number in the callus samples around tibial fractures at 2 weeks after surgery. Results are shown as mean $\pm$ SD. Comparisons were determined by Student's t-test (**P $<$ 0.01). **(c)** Representative images of HE and Masson staining of the fractured rat tibia 4 weeks after Zn–2Cu-0.5Zr alloy implantation. **(d)** Representative images of HE and Masson staining of the fractured rat tibia 8 weeks after Zn–2Cu-0.5Zr alloy implantation.
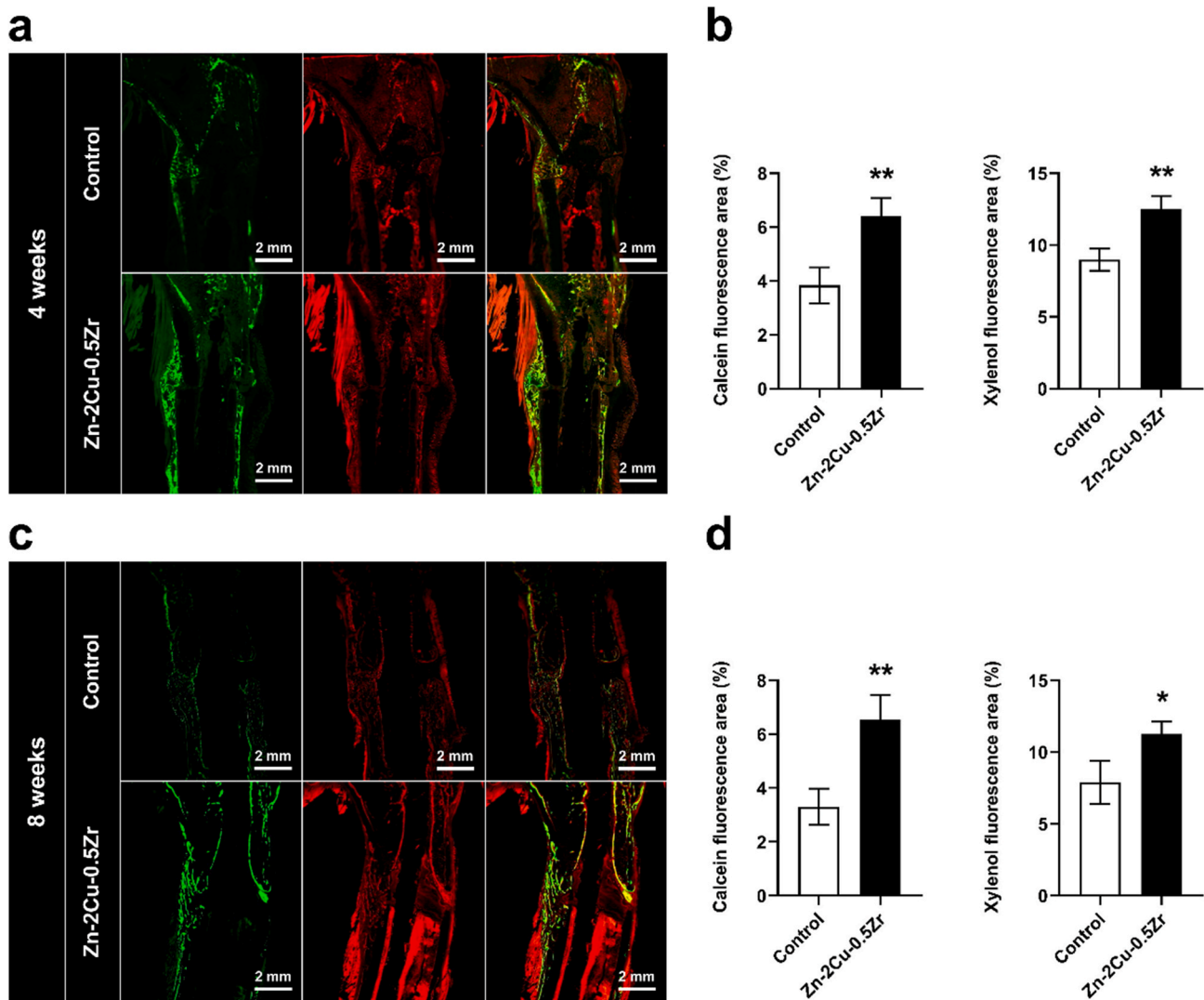
Fig. 10. Bone-remodeling assessment in aged osteoporotic rats. **(a)** Bone-remodeling assessment by calcein/xylenol double labeling in the fractured rat tibia 4 weeks after Zn–2Cu-0.5Zr alloy implantation. **(b)** Rate of bone remodeling is indicated by calcein/xylenol fluorescence area. Results are shown as mean ± SD. Comparisons were determined by Student's *t*-test (**P < 0.01). **(c)** Bone-remodeling assessment by calcein/xylenol double labeling in the fractured rat tibia 8 weeks after Zn–2Cu-0.5Zr alloy implantation. **(d)** Rate of bone remodeling is indicated by calcein/xylenol fluorescence area. Results are shown as mean ± SD. Comparisons were determined by Student's *t*-test (**P < 0.01).
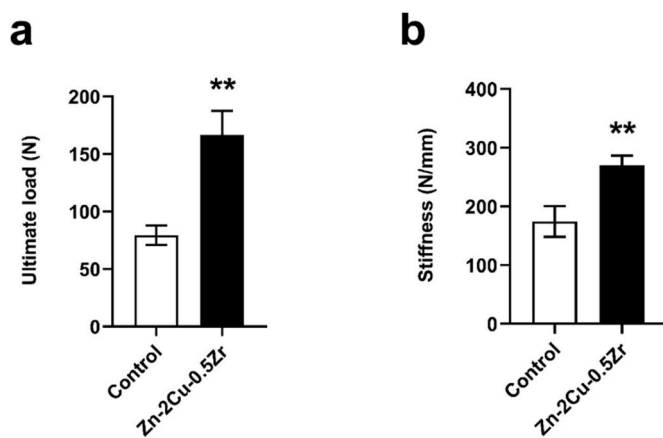
Fig. 11. Biomechanical test of ultimate load force (a) and stiffness (b) of the fractured rat tibia 8 weeks after Zn–2Cu-0.5Zr alloy implantation. Results are shown as mean ± SD. Comparisons were determined by Student's *t*-test (**P < 0.01).

Zn–2Cu-0.5Zr group demonstrated a significant improvement in the strength of the tibial fractures at 8 weeks after surgery, with statistical significance ($p < 0.05$). Specifically, the ultimate load capacity of the fractures in the Zn–2Cu-0.5Zr group was 2.1 times higher than that of the control, while the stiffness was 1.5 times greater, highlighting the enhanced biomechanical properties of the tibial fractures treated with the Zn–2Cu-0.5Zr implant.

4. Discussion

Fracture healing in elderly individuals with osteoporosis is still challenging due to the adverse impact of the aging immune microenvironment. Previous study reported that aging can foster an inflammatory and degenerative microenvironment that impedes fracture healing and contributes to osteoporosis and other diseases [32]. Recently, the interaction between macrophage activity and bone regeneration has been a hot topic for evaluation of advanced biomaterials [33,34]. M1 macrophages fulfill a pro-inflammatory role, phagocytosing cellular debris and dead neutrophils, and secreting inflammatory cytokines like IL-1β, IL-6 and TNF-α. Conversely, a range of osteogenic, angiogenic and

anti-inflammatory cytokines, including BMP2 and IL-10, were generated by M2-type macrophages, which can mitigate inflammatory response and accelerate bone healing [35]. However, an inevitable shift toward M1-type in macrophage polarization can promote inflammatory cytokines with aging, inducing osteoclast differentiation and inhibiting osteoblast differentiation. Therefore, a favorable immune microenvironment is crucial for facilitating the healing of bone injuries, particularly in cases of SOP.

It is acknowledged that Zn serves as a crucial element for the bone metabolism and immune systems. Among the biodegradable metals, Zn-based metals are the better candidates in the field of osteosynthesis implants owing to their degradation rate, corrosion products and biocompatibility [15,16]. Nevertheless, the mechanical characteristics of pure Zn cannot meet the requirements in clinic. The principle of "mechanical-biological" adaptation must be considered when applying Zn-based alloys, with mechanics serving as a prerequisite. Thus, numbers of elements including Mg, Ca, Sr, Li, Mn, Fe, Cu and Ag have been widely explored for binary alloying of Zn [36]. Afterwards, ternary Zn-based alloys were designed to achieve enhanced properties. Studied on the ternary combinations were reported, including Zn–Mg–Ca, Zn–Mg–Sr, Zn–Ca–Sr, Zn–Mg–Fe, Zn–Mg–Mn, Zn–Li–Mg, Zn–Li–Mn, Zn–Li–Sr, Zn-Cu-Fe [29,36–42]. Mg and Li additions have been extensively researched due to their anticipated high biocompatibility.

Cu is also proposed as a promising choice for Zn-based alloys due to its bio-safety. Our previous work had proved that Cu alloying can enhance both strength and ductility of Zn matrix, as well as the antibacterial properties [28]. On the other hand, Zr can yield positive outcome in grain refinement, which might further improve the mechanical and corrosion resistance properties for Zn-based alloy [30]. Furthermore, Zr demonstrates excellent in vivo biocompatibility and low ionic cytotoxicity in vitro, although no research was reported on Zr in Zn-based alloys. For superior performance, a ternary Zn–2Cu-0.5Zr alloy was designed as an optimization based on the Zn–Cu alloy system. We observed that $CuZn_5$ and $Zn_{22}Zr$ appeared as secondary phases after adding Cu and Zr, resulting in more eutectic structures that played a role in grain refinement. Compared to pure Zn, the ZnCuZr alloy system demonstrated significant enhancements in YS, UTS and elongation, indicating that the mechanical properties can be effectively improved through Cu and Zr alloying. Moreover, the initial mechanical properties of Zn–2Cu-0.5Zr alloy met the requirements for clinical applications.

Currently, there is no unified standard system for evaluating the in vitro cytotoxicity of degradable metals and the assessment is influenced by several factors. The impact of Zn^{2+} on cellular response varies depending on external factors such as the cell line used, number of passaged cells and serum type employed [43]. Prior studies have demonstrated that FBS had an influence on the release levels of Zn^{2+} during the extraction process [44]. Direct application of ISO 10993 standard to assess the performance of degradable metals may introduce significant biases due to the large differences between in vivo and in vitro conditions. Wang et al. have recommended revising the current ISO standard and suggested using metal extracts diluted 6–10 times for in vitro cytotoxicity testing [45]. There is an urgent need for the development of a new and integrated evaluation system for assessing the biocompatibility of degradable metals. In this study, we evaluated the in vitro cytotoxicity in BMSCs and MC3T3-E1 cells, which are commonly used in bone tissue research. We tested the extract at 50 % and 10 % diluted concentrations and found that the Zn, Zn–2Cu and Zn–2Cu-0.5Zr alloy extracts had no significant impact on the survival rates of BMSCs and MC3T3-E1 cells. The results from live/dead cell staining and cytoskeleton staining demonstrated that 50 % Zn–2Cu-0.5Zr alloy extracts exhibited negligible toxicity towards BMSCs and MC3T3-E1 cells, with the cells maintaining their normal morphology.

Previous studies have indicated that Zn^{2+} can enhance bone formation and reduce bone resorption [21,22]. However, it is still not clear how Zn^{2+} released from Zn-based alloys affects the polarization state of macrophages and the level of inflammation, which is critical to osteogenesis through mediating the bone immune microenvironment. We investigated the effect of Zn–2Cu-0.5Zr extracts on M1/M2 polarization of macrophages using qRT-PCR, western blotting and immunofluorescence staining in this study. Our findings revealed that the Zn–2Cu-0.5Zr extracts could increase the expression of M2 macrophage markers (CD206, CD163, Arg-1, and IL-10) and suppress the expression of M1 phenotype markers (iNOS, CCR7, IL-6, IL-1β, CD86, and TNF-α). Notably, high concentration of Zn^{2+} (50–80 μM) was found to enhance the M2 phenotype and suppress the M1 phenotype more significantly than low concentrations of Zn^{2+}. Additionally, our findings suggested that Zn^{2+} could reduce the level of ROS produced by macrophages and inhibit the production of inflammatory cytokines, while simultaneously increasing the release of anti-inflammatory cytokines. Specifically, we observed a decrease in the levels of TNF-α and IL-6, alongside an increase in IL-10 as Zn^{2+} concentrations rose. Our findings suggest that Zn^{2+} could facilitate the transition of M1 to M2 polarization in macrophages and the production of anti-inflammatory cytokines, thereby fostering an anti-inflammatory microenvironment conducive to osteogenesis.

Next, we investigated the effect of Zn^{2+}-stimulated macrophages on BMSCs' osteogenic differentiation. The analyses of qRT-PCR and western blott demonstrated that the macrophage-mediated CM significantly augmented the expression associated with early (ALP, Col1, Runx2, OSX) as well as late osteogenic differentiation markers (OPN, OCN). Furthermore, it was observed that the effect of macrophage-mediated CM on BMSCs' osteogenic differentiation was positively correlated with increasing concentrations of Zn^{2+}. The ALP and alizarin red staining also confirmed the afore-mentioned findings. Wnt/β-catenin signaling pathway serves as a crucial regulatory pathway for the proliferation and differentiation of BMSCs [46–48]. Activation of this pathway can stimulate BMSCs' osteogenic differentiation. We also found that Wnt/β-catenin signaling pathway during osteogenic differentiation of BMSCs was activated by the CM. Moreover, our study demonstrated that macrophage-mediated CM played a vital role in this process by counteracting the impact of Zn^{2+}. These results suggest that Zn^{2+} can regulate the M2 polarization of macrophages that leading to secrete more anti-inflammatory cytokines. Consequently, the bone immune microenvironment can further enhance osteogenic differentiation of BMSCs by activating the Wnt/β-catenin signaling pathway.

Research has shown Zn content in the bone decreases significantly with aging, leading to a decline in osteogenic ability and potentially contributing to osteoporosis [20,49,50]. Therefore, restoring Zn intake may alleviate the age-related decline in bone formation. Zn-based metals are promising candidates for the repair of osteoporotic fractures in the elderly. To investigate the effect of Zn–2Cu-0.5Zr implantation on SOP fracture healing, fracture specimens from aged osteoporotic rats were examined via X-ray, micro-CT and histological examination. The results showed that the Zn–2Cu-0.5Zr group stimulated the callus formation and de novo bone formation around the fracture, leading to significantly improved fracture healing at 4 and 8 weeks compared with the control. Histological and sequential fluorescence labeling tests confirmed that the Zn–2Cu-0.5Zr implant facilitated the healing of osteoporotic fractures in aged rats. Additionally, biomechanical testing demonstrated that Zn–2Cu-0.5Zr implantation increased the mechanical strength of tibial fracture healing. Therefore, these outcomes suggest that the promotion of fracture healing by Zn–2Cu-0.5Zr is closely associated with bone immunoregulation mediated by the release of Zn^{2+} from the alloy. Specifically, Zn^{2+} extracts induce M2 polarization in macrophages and the production of anti-inflammatory cytokines, thereby fostering an immune microenvironment beneficial to bone regeneration. This environment enhances the regeneration and repair of bone tissue, ultimately improving both the fracture healing process and the mechanical strength of the healed bone.

5. Conclusion

In this study, we developed a novel biodegradable ZnCuZr alloy system, which exhibited excellent mechanical properties suitable for fracture fixation and repair. The Zn^{2+} extracts from Zn–2Cu-0.5Zr alloy was found to have beneficial immunomodulatory effects that not only modulate the immune inflammatory responses of surrounding tissues during bone repair but also stimulate bone formation. This modulation triggers the release of anti-inflammatory cytokines, thereby accelerating the bone repair process and enhancing the healing of osteoporotic fractures in aged rats. The results underscore the potential of the ZnCuZr alloy system as a promising candidate for biomedical applications in orthopedics, particularly for improving outcomes in the elderly population.

Ethics approval and consent to participate

Animal experiments were approved by the Animal Research Committee of Sichuan University.

CRediT authorship contribution statement

Huanzhong Ji: Writing – original draft, Visualization, Project administration, Methodology, Investigation, Formal analysis, Data curation, Conceptualization. **Gang Shen:** Visualization, Methodology, Formal analysis, Data curation. **Hanghang Liu:** Visualization, Supervision, Software, Formal analysis. **Yao Liu:** Visualization, Supervision, Software, Formal analysis. **Junyu Qian:** Visualization, Supervision, Software, Formal analysis. **GuoJiang Wan:** Writing – review & editing, Project administration, Conceptualization. **En Luo:** Writing – review & editing, Resources, Project administration, Methodology, Conceptualization.

Declaration of competing interest

The authors declare no potential competing interests.

Acknowledgements

Appendix A. Supplementary data

Supplementary data to this article can be found online at https://doi.org/10.1016/j.bioactmat.2024.05.003.

References

[1] T.D. Rachner, S. Khosla, L.C. Hofbauer, Osteoporosis: now and the future, Lancet (London, England) 377 (9773) (2011) 1276–1287.

[2] A. Qadir, S. Liang, Z. Wu, Z. Chen, L. Hu, A. Qian, Senile osteoporosis: the involvement of differentiation and senescence of bone marrow stromal cells, Int. J. Mol. Sci. 21 (1) (2020).

[3] R.J. Pignolo, S.F. Law, A. Chandra, Bone aging, cellular senescence, and osteoporosis, JBMR Plus 5 (4) (2021) e10488.

[4] J.E. Compston, M.R. McClung, W.D. Leslie, Osteoporosis, Lancet (London, England) 393 (10169) (2019) 364–376.

[5] J. Li, R.M.Y. Wong, Y.L. Chung, S.S.Y. Leung, S.K. Chow, M. Ip, W.H. Cheung, Fracture-related infection in osteoporotic bone causes more severe infection and further delays healing, Bone Jnt. Res. 11 (2) (2022) 49–60.

[6] W.H. Cheung, T. Miclau, S.K. Chow, F.F. Yang, V. Alt, Fracture healing in osteoporotic bone, Injury 47 (Suppl 2) (2016) S21–S26.

[7] A.A. Al-Tamimi, C. Quental, J. Folgado, C. Peach, P. Bartolo, Stress analysis in a bone fracture fixed with topology-optimised plates, Biomech. Model. Mechanobiol. 19 (2) (2020) 693–699.

[8] S. Samiezadeh, P. Tavakkoli Avval, Z. Fawaz, H. Bougherara, On optimization of a composite bone plate using the selective stress shielding approach, J. Mech. Behav. Biomed. Mater. 42 (2015) 138–153.

[9] J. O'Connell, C. Murphy, O. Ikeagwuani, C. Adley, G. Kearns, The fate of titanium miniplates and screws used in maxillofacial surgery: a 10 year retrospective study, Int. J. Oral Maxillofac. Surg. 38 (7) (2009) 731–735.

[10] Y. Xie, L. Zhang, Q. Xiong, Y. Gao, W. Ge, P. Tang, Bench-to-bedside strategies for osteoporotic fracture: from osteoimmunology to mechanosensation, Bone Res. 7 (2019) 25.

[11] C. Schlundt, T. El Khassawna, A. Serra, A. Dienelt, S. Wendler, H. Schell, N. van Rooijen, A. Radbruch, R. Lucius, S. Hartmann, G.N. Duda, K. Schmidt-Bleek, Macrophages in bone fracture healing: their essential role in endochondral ossification, Bone 106 (2018) 78–89.

[12] J.P. Barrett, D.A. Costello, J. O'Sullivan, T.R. Cowley, M.A. Lynch, Bone marrow-derived macrophages from aged rats are more responsive to inflammatory stimuli, J. Neuroinflammation 12 (2015) 67.

[13] S.M. Abdelmagid, M.F. Barbe, F.F. Safadi, Role of inflammation in the aging bones, Life Sci. 123 (2015) 25–34.

[14] Y. Yao, X. Cai, F. Ren, Y. Ye, F. Wang, C. Zheng, Y. Qian, M. Zhang, The macrophage-osteoclast Axis in osteoimmunity and osteo-related diseases, Front. Immunol. 12 (2021) 664871.

[15] D. Hernández-Escobar, S. Champagne, H. Yilmazer, B. Dikici, C.J. Boehlert, H. Hermawan, Current status and perspectives of zinc-based absorbable alloys for biomedical applications, Acta Biomater. 97 (2019) 1–22.

[16] H.-S. Han, S. Loffredo, I. Jun, J. Edwards, Y.-C. Kim, H.-K. Seok, F. Witte, D. Mantovani, S. Glyn-Jones, Current status and outlook on the clinical translation of biodegradable metals, Mater. Today 23 (2019) 57–71.

[17] H. Guo, D. Xia, Y. Zheng, Y. Zhu, Y. Liu, Y. Zhou, A pure zinc membrane with degradability and osteogenesis promotion for guided bone regeneration: in vitro and in vivo studies, Acta Biomater. 106 (2020) 396–409.

[18] D. Zhu, Y. Su, M.L. Young, J. Ma, Y. Zheng, L. Tang, Biological responses and mechanisms of human bone marrow mesenchymal stem cells to Zn and Mg biomaterials, ACS Appl. Mater. Interfaces 9 (33) (2017) 27453–27461.

[19] D. Zhu, I. Cockerill, Y. Su, Z. Zhang, J. Fu, K.W. Lee, J. Ma, C. Okpokwasili, L. Tang, Y. Zheng, Y.X. Qin, Y. Wang, Mechanical strength, biodegradation, and in vitro and in vivo biocompatibility of Zn biomaterials, ACS Appl. Mater. Interfaces 11 (7) (2019) 6809–6819.

[20] X. Qu, H. Yang, Z. Yu, B. Jia, H. Qiao, Y. Zheng, K. Dai, Serum zinc levels and multiple health outcomes: implications for zinc-based biomaterials, Bioact. Mater. 5 (2) (2020) 410–422.

[21] E. O'Neill, G. Awale, L. Daneshmandi, O. Umerah, K.W. Lo, The roles of ions on bone regeneration, Drug Discov. Today 23 (4) (2018) 879–890.

[22] M. Yamaguchi, M.N. Weitzmann, Zinc stimulates osteoblastogenesis and suppresses osteoclastogenesis by antagonizing NF-κB activation, Mol. Cell. Biochem. 355 (1–2) (2011) 179–186.

[23] P. Bonaventura, G. Benedetti, F. Albarède, P. Miossec, Zinc and its role in immunity and inflammation, Autoimmun. Rev. 14 (4) (2015) 277–285.

[24] D. Xia, Y. Qin, H. Guo, P. Wen, H. Lin, M. Voshage, J.H. Schleifenbaum, Y. Cheng, Y. Zheng, Additively manufactured pure zinc porous scaffolds for critical-sized bone defects of rabbit femur, Bioact. Mater. 19 (2023) 12–23.

[25] J. Venezuela, M.S. Dargusch, The influence of alloying and fabrication techniques on the mechanical properties, biodegradability and biocompatibility of zinc: a comprehensive review, Acta Biomater. 87 (2019) 1–40.

[26] Z. Tang, J. Niu, H. Huang, H. Zhang, J. Pei, J. Ou, G. Yuan, Potential biodegradable Zn-Cu binary alloys developed for cardiovascular implant applications, J. Mech. Behav. Biomed. Mater. 72 (2017) 182–191.

[27] J. Niu, Z. Tang, H. Huang, J. Pei, H. Zhang, G. Yuan, W. Ding, Research on a Zn-Cu alloy as a biodegradable material for potential vascular stents application, Mater. Sci. Eng. C, Mater. Biol. Appl. 69 (2016) 407–413.

[28] P. Li, W. Zhang, J. Dai, A.B. Xepapadeas, E. Schweizer, D. Alexander, L. Scheideler, C. Zhou, H. Zhang, G. Wan, J. Geis-Gerstorfer, Investigation of zinc-copper alloys as potential materials for craniomaxillofacial osteosynthesis implants, Mater. Sci. Eng. C, Mater. Biol. Appl. 103 (2019) 109826.

[29] W. Zhang, P. Li, G. Shen, X. Mo, C. Zhou, D. Alexander, F. Rupp, J. Geis-Gerstorfer, H. Zhang, G. Wan, Appropriately adapted properties of hot-extruded Zn-0.5Cu-xFe alloys aimed for biodegradable guided bone regeneration membrane application, Bioact. Mater. 6 (4) (2021) 975–989.

[30] Y. Li, C. Wen, D. Mushahary, R. Sravanthi, N. Harishankar, G. Pande, P. Hodgson, Mg-Zr-Sr alloys as biodegradable implant materials, Acta Biomater. 8 (8) (2012) 3177–3188.

[31] D. Chopra, A. Jayasree, T. Guo, K. Gulati, S. Ivanovski, Advancing dental implants: bioactive and therapeutic modifications of zirconia, Bioact. Mater. 13 (2022) 161–178.

[32] T.H. Ambrosi, O. Marecic, A. McArdle, R. Sinha, G.S. Gulati, X. Tong, Y. Wang, H. M. Steininger, M.Y. Hoover, L.S. Koepke, M.P. Murphy, J. Sokol, E.Y. Seo, R. Tevlin, M. Lopez, R.E. Brewer, S. Mascharak, L. Lu, O. Ajanaku, S.D. Conley, J. Seita, M. Morri, N.F. Neff, D. Sahoo, F. Yang, I.L. Weissman, M.T. Longaker, C.K. F. Chan, Aged skeletal stem cells generate an inflammatory degenerative niche, Nature 597 (7875) (2021) 256–262.

[33] Y. Li, Y. Xiao, C. Liu, The horizon of materiobiology: a perspective on material-guided cell behaviors and tissue engineering, Chem. Rev. 117 (5) (2017) 4376–4421.

[34] J. Pajarinen, T. Lin, E. Gibon, Y. Kohno, M. Maruyama, K. Nathan, L. Lu, Z. Yao, S. B. Goodman, Mesenchymal stem cell-macrophage crosstalk and bone healing, Biomaterials 196 (2019) 80–89.

[35] D. Li, K. Chen, H. Tang, S. Hu, L. Xin, X. Jing, Q. He, S. Wang, J. Song, L. Mei, R. D. Cannon, P. Ji, H. Wang, T. Chen, A logic-based diagnostic and therapeutic hydrogel with multistimuli responsiveness to orchestrate diabetic bone regeneration, Adv. Mater. 34 (11) (2022) e2108430.

[36] H. Yang, B. Jia, Z. Zhang, X. Qu, G. Li, W. Lin, D. Zhu, K. Dai, Y. Zheng, Alloying design of biodegradable zinc as promising bone implants for load-bearing applications, Nat. Commun. 11 (1) (2020) 401.

[37] H. Li, H. Yang, Y. Zheng, F. Zhou, K. Qiu, X. Wang, Design and characterizations of novel biodegradable ternary Zn-based alloys with IIA nutrient alloying elements Mg, Ca and Sr, Mater. Des. 83 (2015) 95–102.

[38] X. Liu, J. Sun, Y. Yang, F. Zhou, Z. Pu, L. Li, Y. Zheng, Microstructure, mechanical properties, in vitro degradation behavior and hemocompatibility of novel Zn–Mg–Sr alloys as biodegradable metals, Mater. Lett. 162 (2016) 242–245.

[39] C. Wang, Z. Yu, Y. Cui, Y. Zhang, S. Yu, G. Qu, H. Gong, Processing of a novel Zn alloy micro-tube for biodegradable vascular stent application, J. Mater. Sci. Technol. 32 (9) (2016) 925–929.

[40] X. Liu, J. Sun, F. Zhou, Y. Yang, R. Chang, K. Qiu, Z. Pu, L. Li, Y. Zheng, Micro-alloying with Mn in Zn–Mg alloy for future biodegradable metals application, Mater. Des. 94 (2016) 95–104.

[41] R. Yue, H. Huang, G. Ke, H. Zhang, J. Pei, G. Xue, G. Yuan, Microstructure, mechanical properties and in vitro degradation behavior of novel Zn-Cu-Fe alloys, Mater. Char. 134 (2017) 114–122.

[42] Z. Zhang, B. Jia, H. Yang, Y. Han, Q. Wu, K. Dai, Y. Zheng, Zn0.8Li0.1Sr-a biodegradable metal with high mechanical strength comparable to pure Ti for the treatment of osteoporotic bone fractures: in vitro and in vivo studies, Biomaterials 275 (2021) 120905.

[43] E.R. Shearier, P.K. Bowen, W. He, A. Drelich, J. Drelich, J. Goldman, F. Zhao, In vitro cytotoxicity, adhesion, and proliferation of human vascular cells exposed to zinc, ACS Biomater. Sci. Eng. 2 (4) (2016) 634–642.

[44] P. Li, J. Dai, E. Schweizer, F. Rupp, A. Heiss, A. Richter, U.E. Klotz, J. Geis-Gerstorfer, L. Scheideler, D. Alexander, Response of human periosteal cells to degradation products of zinc and its alloy, Mater. Sci. Eng. C, Mater. Biol. Appl. 108 (2020) 110208.

[45] J. Wang, F. Witte, T. Xi, Y. Zheng, K. Yang, Y. Yang, D. Zhao, J. Meng, Y. Li, W. Li, K. Chan, L. Qin, Recommendation for modifying current cytotoxicity testing standards for biodegradable magnesium-based materials, Acta Biomater. 21 (2015) 237–249.

[46] B. Zhu, F. Xue, G. Li, C. Zhang, CRYAB promotes osteogenic differentiation of human bone marrow stem cells via stabilizing β-catenin and promoting the Wnt signalling, Cell Prolif. 53 (1) (2020) e12709.

[47] X. Cui, Y. Zhang, J. Wang, C. Huang, Y. Wang, H. Yang, W. Liu, T. Wang, D. Wang, G. Wang, C. Ruan, D. Chen, W.W. Lu, W. Huang, M.N. Rahaman, H. Pan, Strontium modulates osteogenic activity of bone cement composed of bioactive borosilicate glass particles by activating Wnt/β-catenin signaling pathway, Bioact. Mater. 5 (2) (2020) 334–347.

[48] W. Shi, C. Xu, Y. Gong, J. Wang, Q. Ren, Z. Yan, L. Mei, C. Tang, X. Ji, X. Hu, M. Qv, M. Hussain, L.H. Zeng, X. Wu, RhoA/Rock activation represents a new mechanism for inactivating Wnt/β-catenin signaling in the aging-associated bone loss, Cell Regen. 10 (1) (2021) 8.

[49] X. Fu, Y. Li, T. Huang, Z. Yu, K. Ma, M. Yang, Q. Liu, H. Pan, H. Wang, J. Wang, M. Guan, Runx2/Osterix and zinc uptake synergize to orchestrate osteogenic differentiation and citrate containing bone apatite formation, Adv. Sci. 5 (4) (2018) 1700755.

[50] J. Zheng, X. Mao, J. Ling, Q. He, J. Quan, Low serum levels of zinc, copper, and iron as risk factors for osteoporosis: a meta-analysis, Biol. Trace Elem. Res. 160 (1) (2014) 15–23.